ACS OMEGA

http://pubs.acs.org/journal/acsodf

Article

Cold Crystallization and the Molecular Structure of Imidazolium-Based Ionic Liquid Crystals with a *p*-Nitroazobenzene Moiety

Katsuma Ishino, Hajime Shingai, Yasuyuki Hikita, Isao Yoshikawa, Hirohiko Houjou, and Katsunori Iwase*

Cite This: *ACS Omega* 2021, 6, 32869−32878

Read Online

ACCESS | Metrics & More | Article Recommendations | Supporting Information

ABSTRACT: The cold crystallization mechanism of 1-{[4′-(4″-nitrophenylazo)phenyloxy]}-hexyl-3-methyl-1*H*-imidazol-3-ium tetrafluoroborate ionic liquid crystal was investigated based on thermal analysis, structural analysis, infrared spectroscopy, and quantum chemical calculations. By conducting thorough structural characterization, we found that the prerequisite for cold crystallization is the irreversible molecular conformational alteration induced by the initial heating of the as-grown crystal into a smectic liquid crystal. The originally linear cation molecule bends and forms a step-stair conformation that persists throughout the subsequent heating and cooling processes as phase transition occurs from the crystal phase to the liquid crystal phase and then to the isotropic liquid phase. The formation of cold crystal occurs because of the choice of molecular stability over crystalline stability. Given the exothermic anomaly exhibited upon heating generic crystals to cold crystals, these findings demonstrate the promising potential of this ionic liquid crystal for thermal energy storage applications.

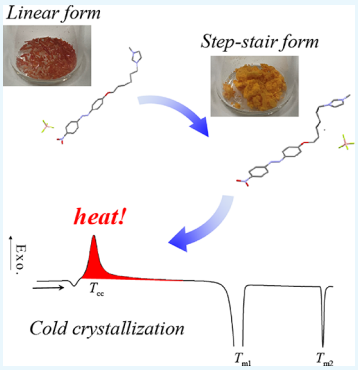

1. INTRODUCTION

Cold crystallization is a unique phenomenon in which crystallization accompanying exothermal anomaly occurs when a material is heated within a temperature range below its melting point. Differential scanning calorimetry (DSC) analysis of crystalline materials that exhibit cold crystallization has demonstrated that the liquid state leads to a deep supercooled state without crystallization during cooling, and cold crystallization occurs via glass transition on subsequent heating. Therefore, the state of the material prior to cold crystallization is storing excess thermal energy. Several studies on thermal energy-storing materials have been inspired by this cold crystallization phenomenon.[1−4]

Most materials that exhibit cold crystallization have a slow rate of crystallization from the liquid to the solid phase. Previous studies have typically investigated polymeric materials,[5−7] but recent research has focused on smaller molecular materials, such as ionic liquids,[8,9] liquid crystals,[10−12] organic materials,[3,13−17] and metal complexes.[2,18−26] Most of these studies focus on the thermal behavior of these materials (e.g., macroscopic heat absorption and emission), and only a few studies have investigated the molecular structural features associated with such thermal behavior or presented guidelines for designing molecules applicable for thermal energy storage.[2,18,19,26]

Previous studies on mono-molecular crystalline materials (e.g., nickel−Schiff base complexes) have provided two important guidelines for designing molecules that exhibit cold crystallization.[2,18,19] First, the molecule should contain a flexible moiety to increase the degree of molecular motion. Second, the liquid (molten) state should consist of several isomers that can undergo structural changes to disrupt the uniformity of the system. Application of these guidelines have successfully led to the realization of cold crystals in two-component molecular systems[25] and compounds showing proton tautomerization.[19]

From a molecular structural perspective, Honda *et al.* highlighted the need for the molecules to contain a π-conjugated rigid core and flexible alkyl chains for cold crystallization.[26] It is not surprising that many such compounds exhibit properties characteristic of liquid crystals, i.e., anisotropic molecules phase transition to and from a partial long-range order mediated by molecular motion.[27] In this sense, a subset of compounds known as ionic liquid crystals, in which the mesogenic units are charged ions exhibiting high degrees of translational and rotational mobilities together with partial orientational and positional orders, are especially attractive candidates for cold crystallization.[28−33] This is because of the coexistence of strong ionic character and the molecular structural degree of freedom, allowing enhanced manipulation of the thermodynamic properties of cold crystallization.[34−37] We note that ionic liquid crystals are distinguished from ionic liquids, which form a larger set of

Received: September 3, 2021
Accepted: November 10, 2021
Published: November 22, 2021

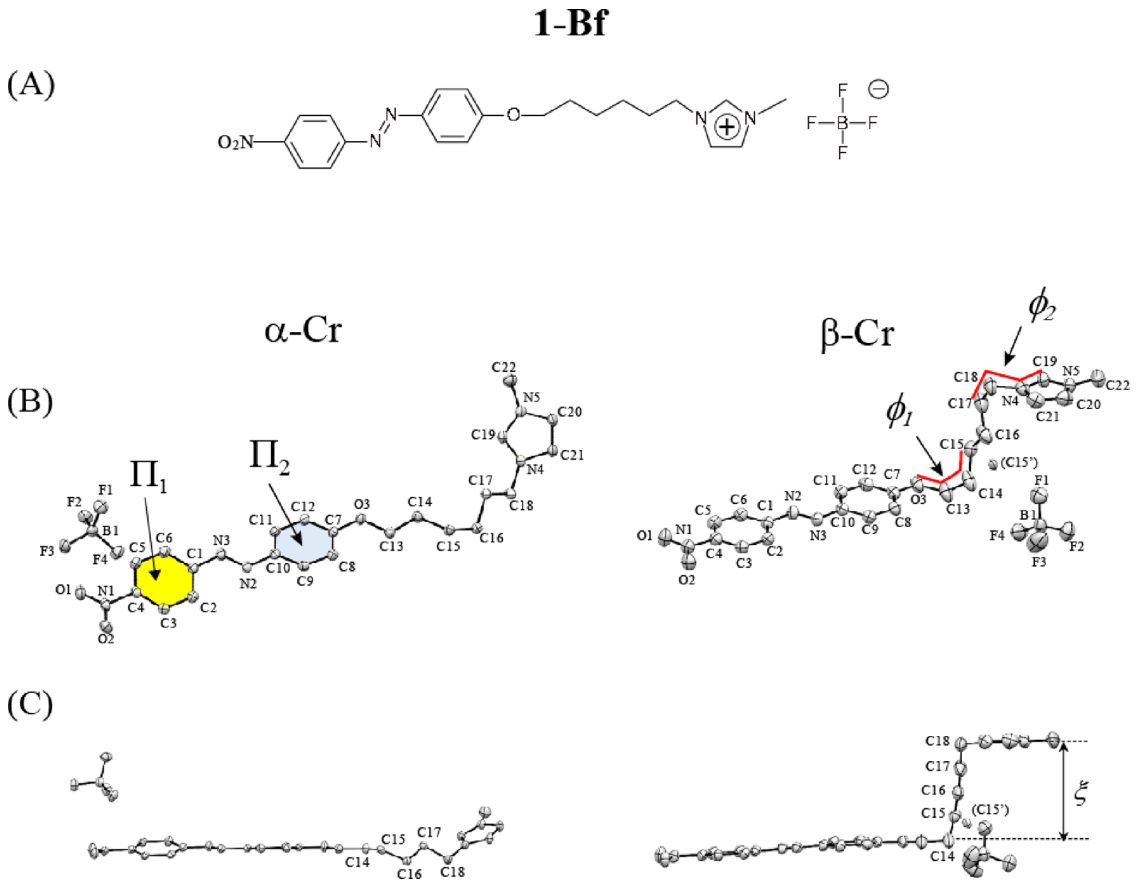

Figure 1. (A) Molecular structure of **1-Bf** and (B) atomic numbering and ORTEP drawings of α-Cr (Left) and β-Cr (Right) determined from single-crystal X-ray diffraction, where the hydrogen atoms are omitted for clarity. The molecules were viewed along the (B) face and (C) edge of the coordination plane. The planes, angles, and vertical distance are defined as follows: Π_1, C1-C6 ring plane in the azobenzene moiety; Π_2, C7-C12 ring plane in the azobenzene moiety; ϕ_1, the dihedral angle, O3−C13−C14−C15; ϕ_2, the dihedral angle, C17−C18−N4−C19; ξ, the vertical distance between Π_2 and C18 on the lower edge-on view.

compounds consisting of ions but not necessarily presenting the character of liquid crystals.[38−44] Ionic liquid crystals tend to have melting points below 100 °C (373 K),[32−34] which is favorable for thermal energy applications below 200 °C (473 K).[45] However, their glass transition temperatures (T_g) are approximately two-thirds of their melting point temperatures (T_m), which is generally referred to as the two-third rule.[46−48] Thus, a material with a melting point around 100 °C (373 K) likely shows a T_g below room temperature −24 °C (249 K). For thermal energy storage (retention) applications (for example, use of exhaust heat in automobiles) at room temperature, such materials would be practically unstable and lead to abnormal heat dissipation as they would be in the liquid phase.

Based on the above argument, we focused on the cold crystallization of an ionic liquid crystal that partially crystallizes during the cooling process, 1-{[4′-(4″-nitrophenylazo)-phenyloxy]}hexyl-3-methyl-1*H*-imidazol-3-ium tetrafluoroborate (**1-Bf**). This molecule has an azobenzene core and a flexible alkyl group with an imidazolium moiety at the end.[37] It exhibits deep supercooling of the smectic phase during cooling, crystallization near room temperature, and cold crystallization upon reheating. Therefore, **1-Bf** is a promising thermal energy storage material that ensures thermal cycling stability at room temperature. However, the structural evolution leading to the formation of cold crystals has not been elucidated for this compound.

This study aimed to determine the molecular and crystal structure of the cold crystal phase in **1-Bf** and elucidate its cold crystallization mechanism based on thermal analysis, structural analysis, infrared spectroscopy, and quantum chemical calculations.

2. RESULTS AND DISCUSSION

2.1. Structural Analysis of the Polymorphic Crystals.

Single-crystal XRD of **1-Bf** revealed a structure with an azobenzene moiety and an imidazolium moiety bonded by an alkyl chain (Figure 1A). The molecules in the α-Cr exhibited a linear alkyl chain between the azobenzene and imidazolium moieties (Figure 1B), which is referred to as the linear form (L-form). On the other hand, the molecules in the β-Cr showed a single bend between the azobenzene and imidazolium moieties, which we call as the step-stair form (SS-form).

The least-square planes of the two aromatic rings of the azobenzene moiety were defined as Π_1 (C1-C6) and Π_2 (C7-C12). In α-Cr, the angle between the normal vectors of Π_1 and Π_2 was 16.6°. The dihedral angle O3−C13−C14−C15 (C17−C18−N4−C19) was defined as ϕ_1 (ϕ_2) and measured as ϕ_1 = 177.5° (ϕ_2 = −58.0°) in α-Cr as shown in Figure 1B (left). The vertical distance (ξ) between Π_2 and C18 was 0.8 Å (Figure 1C, left). On the other hand, in β-Cr, the angle between the Π_1 and Π_2 rings was 1.2°, indicating that there is negligible twist between these two surfaces. The two dihedral

https://doi.org/10.1021/acsomega.1c04866
ACS Omega 2021, 6, 32869−32878

angles were ϕ_1 = 67.7° and ϕ_2 = 59.8°, as shown in Figure 1B (right). The vertical distance (ξ) was 4.8 Å (Figure 1C, right). The crystal structures of α-Cr and β-Cr projected on the *a*- and *b*-axes are shown in Figure S1A−D, respectively.

To study the structural changes associated with cold crystallization, the crystal structure of the synthesized bulk sample must be determined. The powder patterns simulated based on the determined crystal structures of the three selected single crystals were in excellent agreement with those of the bulk sample obtained via SAXS and XRD analyses at room temperature (Figure 2). Note that we observed no apparent changes of the cold crystal sample as it was cooled while sampling from the DSC pan (Figure S2).

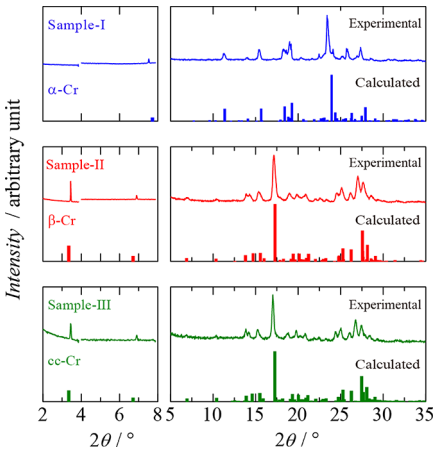

Figure 2. Experimental SAXS-XRD analysis of Sample-I (blue line), Sample-II (red line), and Sample-III (green line) at room temperature compared to the calculated patterns determined independently based on the crystal structures for α-Cr, β-Cr, and cc-Cr. The 2θ values correspond to those using λ of Cu Kα radiation.

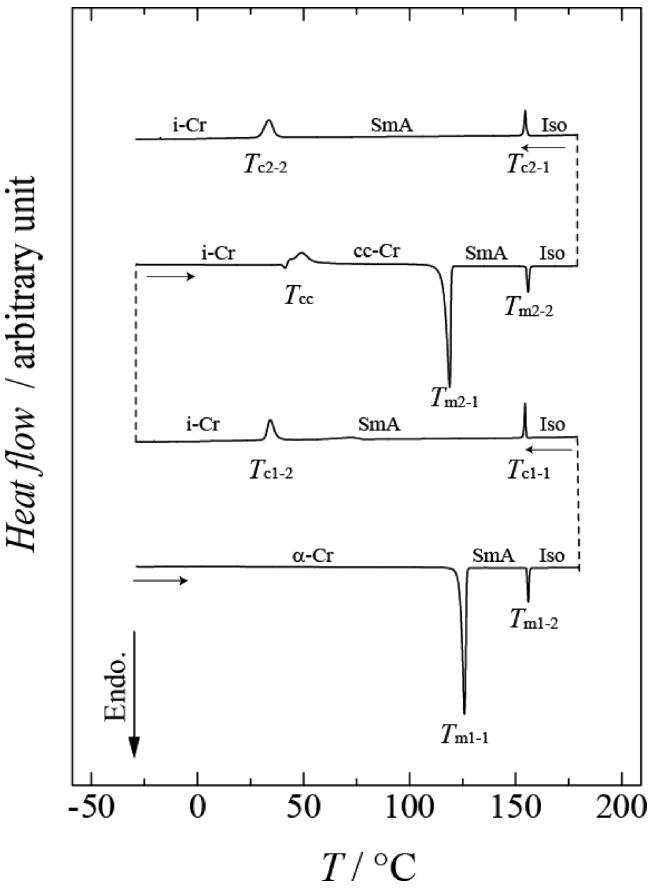

Figure 3. DSC traces of **1-Bf** at a scanning rate of ±5.0 °C min^{-1}, where fusion is denoted by T_{m1-1}, T_{m1-2}, T_{m2-1}, and T_{m2-2}, cold crystallization by T_{cc}, and crystallization by T_{c1-1}, T_{c1-2}, T_{c2-1}, and T_{c2-2}. The starting sample was Sample-I (α-Cr).

Regarding the structure of the three crystals, the bulk samples of the β-Cr (Sample-II) and cc-Cr (Sample-III) were almost identical, whereas the bulk samples of the α-Cr (Sample-I) differed from these two. The packing similarity was confirmed using Mercury software,[49] and the β-Cr and cc-Cr produced an RMS score of 0.060 (15 out of 15 molecules in common).

2.2. Thermal Behavior. DSC analysis of the initial crystal revealed that **1-Bf** underwent a series of phase transitions (Figure 3). They are, namely, from the initial crystal phase (α-Cr) to the liquid crystal phase (SmA) (T_{m1-1}: 123.6 °C) and melting from SmA to an isotropic liquid phase (Iso) (T_{m1-2}: 155.1 °C) during the first heating process. Upon cooling, a phase transition from Iso to SmA (T_{c1-1}: 155.0 °C) and crystallization from SmA (T_{c1-2}: 37.6 °C) to an intermediate supercooled crystalline phase i-Cr, the details of which will be given later, were observed. The second heating cycle involved recrystallization (i.e., cold crystallization, T_{cc}: 42.2 °C) that transformed the cc-Cr to SmA (T_{m2-1}: 115.9 °C) and finally to Iso (T_{m2-2}: 154.9 °C). We note that a glass transition (T_g) was not observed in the cooling process, and the endothermic peak anomaly observed immediately before the exothermic anomaly upon heating around T_{cc} is identified as a glass transition partially coupled to the cold crystallization, based on a series of sweep rate dependent thermal analysis (Figure S4).

The detailed thermodynamic characteristics of each thermal anomaly are given in Table S1. The cold crystal in the second heating cycle exhibited a melting point (T_{m2-1}) 7.7 °C lower than that of the initial crystal (T_{m1-1}), indicating that the cold crystal was thermodynamically less stable than the initial crystal (Figure 3 and Table S1). The thermal behavior of the crystal beyond the third thermal cycle was similar to the second cycle. These observations, reproducing the thermal behavior reported by Zhang *et al.*,[37] set a firm platform on which to investigate the structural evolution of this ionic liquid during the heat cycles.

2.3. Structural Evolution during the Cold Crystallization Process. The relationship between the thermal behavior leading to cold crystallization and the corresponding crystal structures is a very important aspect of the cold crystallization mechanism. The structural relationship between the initial crystal phase, the crystal phase while cooling, and the cold crystal phase is of particular interest. In this study, we focused on the molecular conformation constituting the crystal and unveiled its thermal and the crystallization behaviors comprehensively by employing SAXS, XRD-DSC, and FTIR analyses and quantum chemical calculations.

The SAXS and XRD-DSC results of the first cooling process are presented in Figure 4A−C. The starting sample was Sample-I (α-Cr). The SAXS pattern exhibited a peak at 2θ = 7.7 ° in the initial crystalline state at room temperature (Figure 4A-i). The higher angle diffraction pattern of the initial crystal state disappeared upon heating to approximately 180 °C, indicating the loss of long-range order in the system (Figure

https://doi.org/10.1021/acsomega.1c04866
ACS Omega 2021, 6, 32869−32878

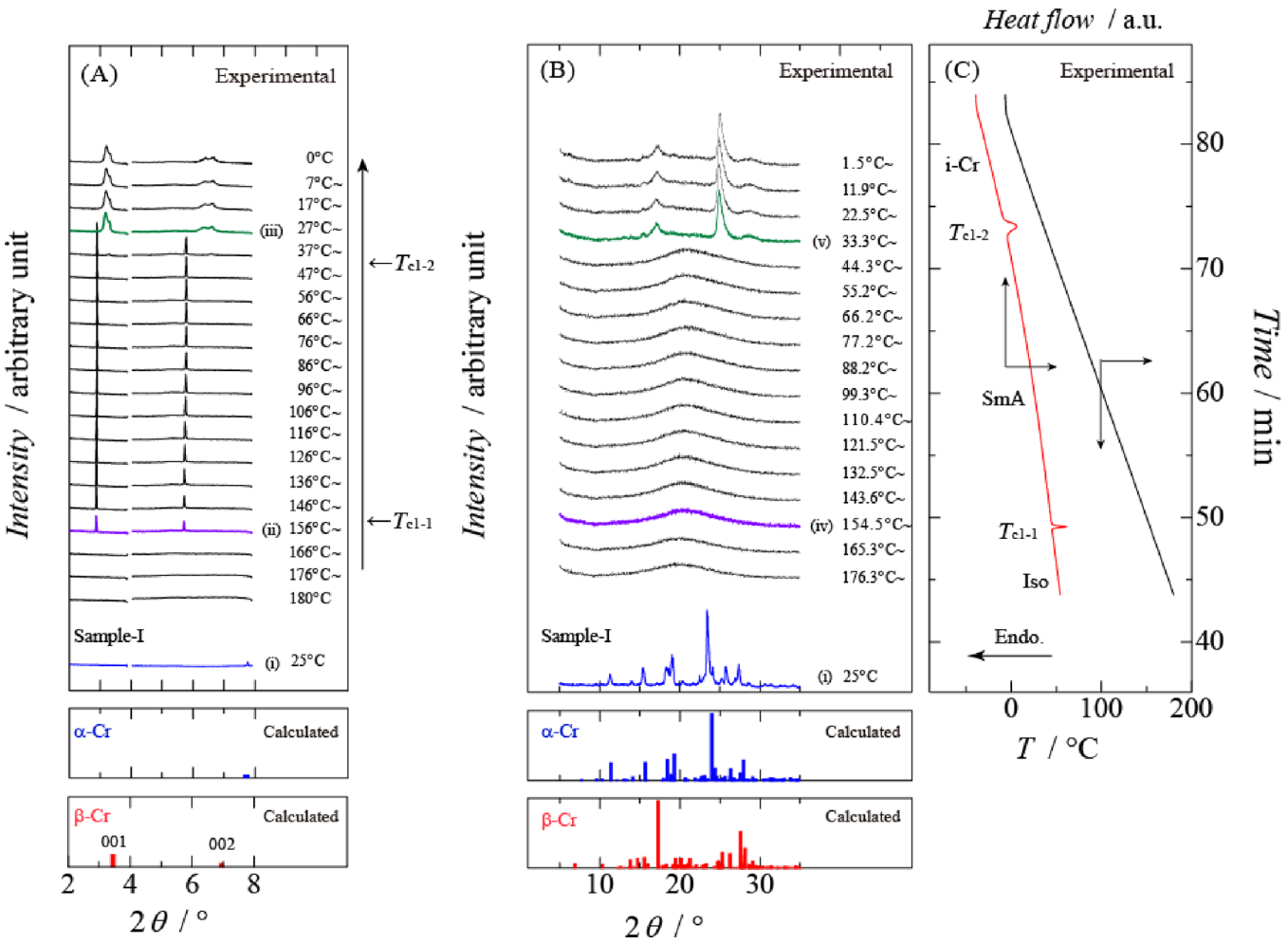

Figure 4. (A) SAXS, (B) XRD-DSC analysis, and (C) DSC (black line: temperature; red line: heat flow) of **1-Bf** during the first cooling process compared with the calculated diffraction patterns based on the independently determined initial single-crystal structure. The 2θ values correspond to those using λ of Cu Kα radiation. The intensities of the SAXS ($4 \leq 2\theta/^\circ \leq 8$) measurements are multiplied by a factor of two for clarity. The starting sample was Sample-I (α-Cr).

4B-iv). During the cooling process of the sample from approximately 180 °C, the sample underwent several transitions. Upon cooling from Iso to SmA, a strong pair of peaks appeared below T_{c1-1} (155.0 °C) in the SAXS profile (Figure 4A-ii), which persisted till approximately T_{c1-2} (37.6 °C) (Figure 4A). We attributed these peaks to the diffraction from the layer normal in the SmA phase, given that their positions (2θ = 2.8 and 5.7°) are close to the diffraction from the (001) and (002) planes in the crystalline phase. The broad pattern in the higher angle XRD persisted between T_{c1-1} and T_{c1-2} (Figure 4B). Interestingly, continued cooling below T_{c1-2} induced a transition from SmA to i-Cr, leading to the emergence of a diffraction pattern, namely, the broadened SAXS peaks at 2θ = 3.0−3.3 and 6.0−6.6 °, suggestive of *c*-axis contraction to varying degrees (Figure 4A-iii), distinct from that of the initial crystal (α-Cr). The peak broadening in SAXS is observed upon cooling the SmA phase below T_{c1-2} and is concomitant with the development of the in-plane long-range order as seen from the broad peaks in the range of 15−20° and 25−30° in Figure 4B. Therefore, we believe that the sample consists of crystals with varying lattice constants in this phase, which is giving rise to the peak broadening in SAXS. We note that this i-Cr phase also consists of amorphous regions as evidenced by the glass transition upon heating prior to the cold crystallization at T_{cc} in the DSC curve, which favorably stabilize the crystals with varying lattice constants. Interestingly, the lattice spacing estimated from the SAXS peaks in i-Cr lies in between the value for SmA and cc-Cr (β-Cr), consistent with the role of i-Cr acting as a precursor to the formation of the cold crystal from the uniaxially ordered phase. These SAXS and XRD results strongly suggest the formation of a different crystalline phase. Upon heating, no change in the diffraction pattern was observed until approximately 40 °C. The exothermal anomaly (cold crystallization) observed at temperatures exceeding T_{cc} (42.2 °C) via T_g was accompanied by the appearance of a sharp diffraction pattern resembling the β-Cr (Figure 5B-ix). In the SAXS region above T_{cc}, the broadened SAXS peaks in the i-Cr phase shifted to higher angles in the 001 and 002 reflections of β-Cr (cc-Cr) (Figure 5A-vi and Figure S5). In addition, the exothermal anomaly at T_{cc} in the DSC pattern (Figures 3 and 5C) consists of two peaks suggestive of a two-step cold crystallization process associated with the contraction of the SmA layer spacing.

Crystallization generally involves crystal nucleation and growth of nucleus.[50,51] Two characteristic features of the cold crystallization process are the promotion of nucleation as the supercooled glassy state gradually gains mobility with increase in temperature and the presence of a maximum temperature

https://doi.org/10.1021/acsomega.1c04866
ACS Omega 2021, 6, 32869−32878

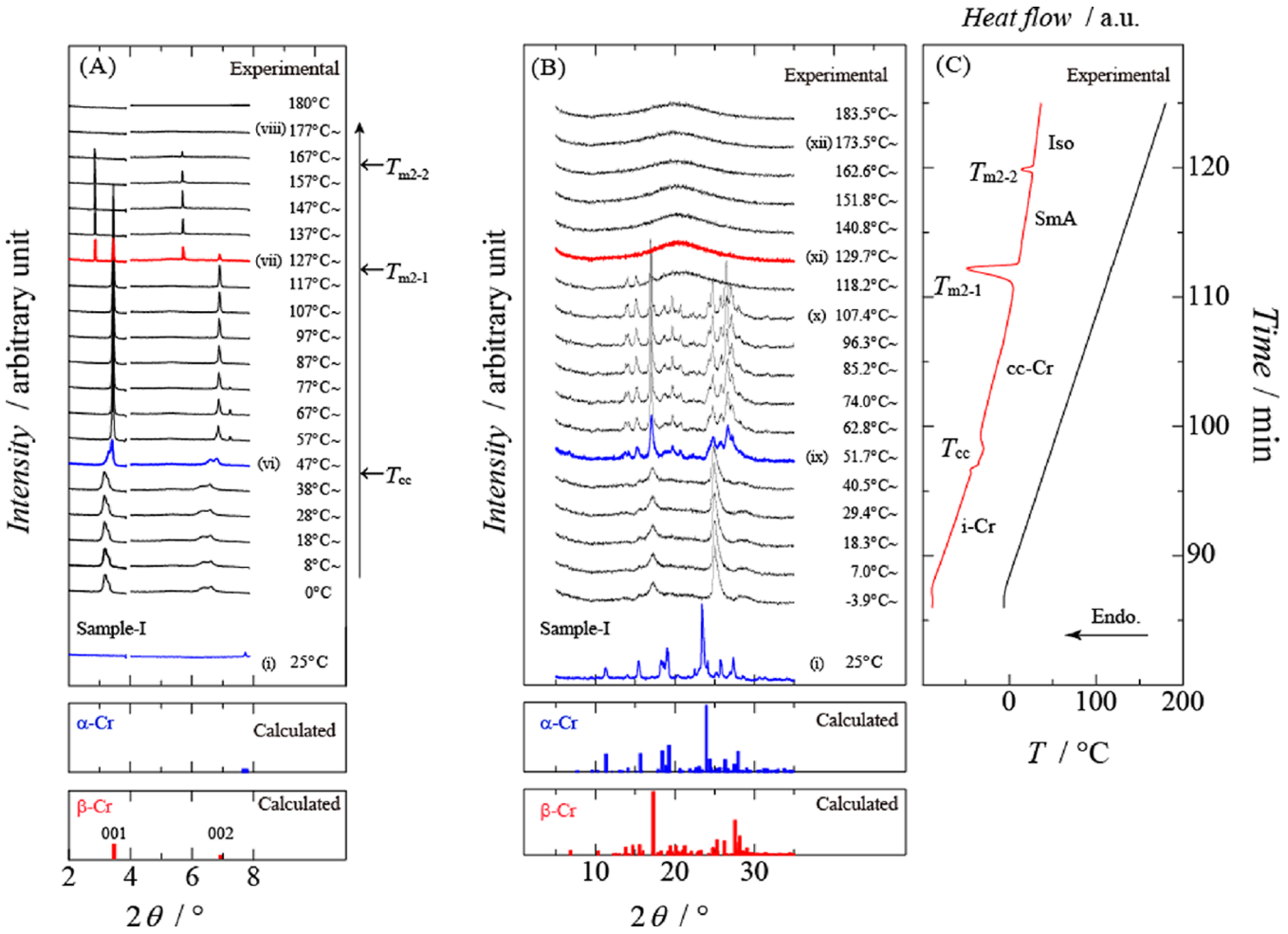

Figure 5. (A) SAXS, (B) XRD-DSC analysis, and (C) DSC (black line: temperature; red line: heat flow) of **1-Bf** during the second heating process compared with the calculated patterns based on the independently determined initial single-crystal structures. The 2θ values correspond to those using λ of Cu Kα radiation. The intensities for a part of the SAXS ($4 \leq 2\theta$ /° ≤ 8) measurements are multiplied by a factor of two for clarity. The starting sample was Sample-I (α-Cr).

for nucleation above which the cold crystallization process is diffusion limited.[52,53] In this study, nucleation is fast judging from the small separation between T_g and T_{cc} and the diffusion-controlled region is rate-limiting, which is evident from the wide temperature range of the T_{cc} peak (around 40 to 70 °C). This is reasonable given the large difference in the size of the cations and the anions, as well as the steric hindrance of the cations through which the anions must diffuse. Specifically, nuclei were formed from SmA and subsequently grew into i-Cr by aggregating into microcrystals that served as the seed crystal for the growth of the β-Cr. In other words, the i-Cr acted as an intermediate crystal phase for the formation of the cc-Cr (β-Cr). Further heating of cc-Cr (β-Cr) resulted in a transition to SmA stabilized between T_{m2-1} (115.9 °C) and T_{m2-2} (154.9 °C), which was accompanied by a shift in the 001 and 002 reflections in the cc-Cr (β-Cr) (Figure 5A-vii) and the disappearance of higher angle diffraction peaks (Figure 5B-xi). Finally, above T_{m2-2}, no diffraction peaks were observed in the entire 2θ range, indicating a transition into the Iso (Figure 5A-viii,B-xii).

To gain insights into the molecular conformation variation and its stability during these phase transitions, we employed the FTIR results and quantum chemical calculations (ONIOM calculation).

The experimental FTIR spectra in the as-grown Sample-I (α-Cr) and Sample-II (β-Cr) crystals showed similar spectra in the 1400−800 cm^{-1} range, but noticeable differences were observed around 900−800 cm^{-1}, which we attribute to the molecular conformation of the cations (Figure 6C−A). The four vibrational modes in α-Cr observed around 900−800 cm^{-1} in Figure 6A′−C′ can be attributed to the following: the out-of-plane C−H stretching of the azobenzene moiety (867 and 859 cm^{-1}), the C−H bending of the alkyl chain (859 and 846 cm^{-1}), and the out-of-plane C−H stretching of the imidazolium moiety (846 and 832 cm^{-1}). The two peaks in β-Cr are attributed to the following: the out-of-plane C−H stretching of the azobenzene moiety and the C−H bending of the alkyl chain (857 cm^{-1}), and the C−H bending of the alkyl chain and the out-of-plane C−H stretching of the imidazolium moiety (840 cm^{-1}). Combined with the negligible energy difference (~1 kJ mol^{-1}) between the two conformations obtained from the calculations, these results suggest that the intermolecular Coulombic interaction plays a crucial role in the series of crystallization processes (Table S4).[54,55]

Upon first heating at approximately T_{m1-1}, at which point the α-Cr transitions into SmA, the FTIR spectra above T_{m1-1} closely matched that of in β-Cr, suggesting that a conformational alteration occurred, which changed the L-form in α-Cr

https://doi.org/10.1021/acsomega.1c04866
ACS Omega 2021, 6, 32869−32878

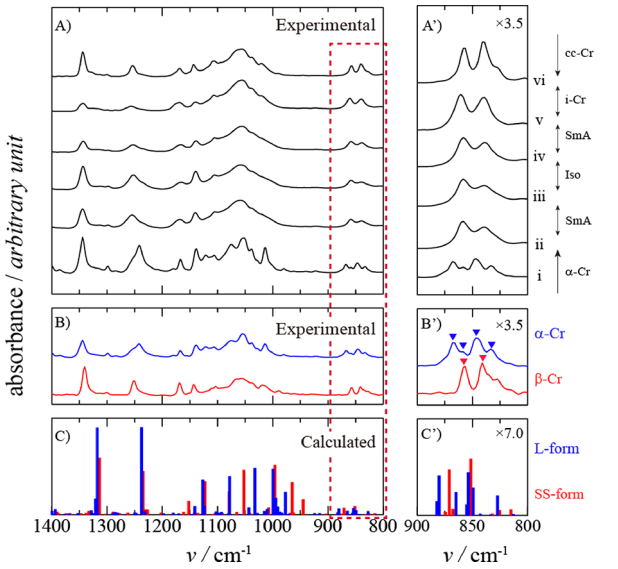

Figure 6. FTIR spectra of **1-Bf** taken during (A) the first thermal cycle and the second heating process at (i) room temperature and immediately after the phase transitions at (ii) T_{m1-1}, (iii) T_{m1-2}, (iv) T_{c1-1}, (v) T_{c1-2}, and (vi) T_{cc}. (B) Comparison of the FTIR spectra for α-Cr and β-Cr. (C) Calculated IR spectra in L-form and SS-form molecules are shown for comparison. (A′−C′) Magnified region of interest (red dotted area at 900−800 cm^{-1}) from (A−C). The starting sample was Sample-I (α-Cr).

to the SS-form in β-Cr. The subsequent series of transitions from SmA to Iso and cooling back to SmA exhibited no spectral shifts in the FTIR spectra, indicating that Iso and SmA maintained the same SS-form conformation. Upon further cooling from SmA to i-Cr and finally to β-Cr, the two peaks (857 and 840 cm^{-1}) did not show a significant change, indicating that the SS-form was maintained throughout the crystalline phases. The absence of conformational alteration after the initial transition at T_{m1-1} confirms that the c-axis contraction observed in the intermediate crystal i-Cr was not due to the presence of the two forms of cations but likely due to the distribution of the SS-form cation positions. From these results, we identified the β-Cr phase as the cc-Cr and concluded that the crucial process in the formation of cold crystals with the β-Cr structure is the ordering into an intermediate crystalline phase (i-Cr) during cooling after the melting of the initial crystal into Iso.

In summary, the cold crystal of **1-Bf** consists of cations in the step-stair conformation that is irreversibly formed after the first melting of the initial crystal, α-Cr, at T_{m1-1}. This molecular conformation persists throughout the subsequent phases: Iso, SmA, i-Cr, and cc-Cr. The intermediate phase i-Cr is a crystalline phase capable of hosting a wide range of displacements in cation positions, which act as the nuclei in the following cold crystallization process. Overall, the cold crystallization of **1-Bf** is a crystallization process that selects the step-stair conformation that is more metastable than the linear form in the initial crystal.

3. CONCLUSIONS

The cold crystallization of **1-Bf** was investigated based on thermal analysis, structural analysis, infrared spectroscopy, and quantum chemical calculations. We found that the structure of the cold crystal phase of **1-Bf** consisted of cations in the step-stair conformation that is formed when the as-grown crystal synthesized in dichloromethane consisting of a linear conformation transforms into a smectic liquid crystal. Subsequent cooling of the liquid crystal phase maintains the bulky step-stair conformation and results in a disordered crystal that can accommodate a wide range of displacements in the cation positions. It is this energy stored in the frustrated crystal that causes cold crystallization upon reheating.

From the perspective of thermal energy utilization, materials with melting points between 100 and 150 °C have T_g's below room temperature according to the two-third rule. For example, a material used in automobiles to store waste heat would be in a supercooled liquid state at room temperature. This would lead to practical instability due to abnormal heat dissipation through solidification triggered by several factors, such as vibration owing to the opening and closing of doors. Instead, the intermediate crystals formed in **1-Bf** offer stable thermal energy storage near room temperature. The thermal energy associated with cold crystallization would be best utilized if minimal heat was generated by crystallization during cooling. Future research should be conducted to fine-tune the molecular structure to increase the heat capacity associated with cold crystallization, thereby improving the reliability and controllability of this phenomenon in several applications.

4. EXPERIMENTAL SECTION

4.1. Sample Synthesis. 1-{[4′-(4″-Nitrophenylazo)-phenyloxy]}hexyl-3-methyl-1*H*-imidazol-3-ium bromide (**1-Br**) was synthesized according to the previously reported procedure.[37] The total yield was 52%. **1-Br** (2.0 g, 4.1 mmol) was dissolved in 30 mL of H_2O. A solution of $LiBF_4$ (2.0 g, 21 mmol) in 20 mL of H_2O was added dropwise to the **1-Br** solution. This mixture was stirred for 1 h at 80 °C under a N_2 atmosphere. The precipitate was filtered from the solution and washed several times with water. The crude product was dissolved in dichloromethane, recrystallized, and dried under vacuum for 24 h to obtain pure orange needle-shaped crystals of **1-Bf** (1.3 g, 65%), which we define as the α phase (α-Cr). A half portion of the initial crystals was further dissolved in ethanol and recrystallized (0.5 g, 79%), which we define as the β phase (β-Cr). All reagents and solvents used for the synthesis were purchased from TCI Co., Ltd., Japan, and used without further purification. Elemental analyses were carried out on a Thermo Scientific FLASH 2000 elemental analyzer. The product was dissolved in tetrahydrofuran and mixed with the matrix solution for mass spectroscopy measurements. The mixture solution (~1 μL) was dropped on the measuring plate and dried before conducting matrix-assisted laser desorption ionization-time-of-flight mass spectrometry (MALDI-TOF MS) analysis (ultrafleXtreme, Bruker Japan). All spectra were measured in both positive ion mode and negative ion mode in the reflector mode, where a 355 nm Nd-YAG laser was used to ionize the sample. All spectra were averaged from 5000 laser shots irradiated over the entire sample area. The product was further characterized after dissolving in deuterated chloroform ($CDCl_3$) by ^1H nuclear magnetic resonance (NMR) and ^{13}C NMR spectroscopic analyses (AVANCEIII-600 with Cryo Probe, Bruker Biospin), where 600 MHz was used for ^1H NMR. We confirmed the purity of ionic liquid **1-Bf** by ^1H NMR and ^{13}C NMR (Figures S6 and S7). The melting point was determined as the onset temperature during heating for the first cycle of the DSC measurements. Consequently, the orange needle-shaped crystals (α-Cr) with a melting point of

https://doi.org/10.1021/acsomega.1c04866
ACS Omega 2021, 6, 32869−32878

122.5 °C (first heating process) exhibited the following characteristics: ^{1}H NMR (600 MHz, $CDCl_3$, δ): 9.04 (1H, s, imidazolium ring), 8.34−8.36 (2H, d, J = 9.0 Hz, Ar−H), 7.96−7.98 (2H, d, J = 9.0 Hz, Ar−H), 7.93−7.95 (2H, d, J = 9.0 Hz, Ar−H), 7.20 (2H, s, imidazolium ring), 7.00−7.02 (2H, d, J = 9.0 Hz, Ar−H), 4.23 (2H, t, J = 7.5 Hz, N−CH_2), 4.06 (2H, t, J = 6.0 Hz, OCH_2), 3.98 (3H, s, N−CH_3), 1.95 (2H, m, CH_2), 1.83 (2H, m, CH_2), 1.58 (2H, m, CH_2), 1.45 (2H, m, CH_2). ^{13}C NMR (150 MHz, $CDCl_3$, δ): 25.39, 25.86, 28.80, 29.97, 36.62, 50.26, 68.02, 114.95, 121.67, 123.14, 123.17, 124.76, 125.68, 137.45, 146.89, 148.26, 156.07, 162.76. Elemental analysis calculated for $C_{22}H_{26}N_5O_3BF_4$: C, 53.35; H, 5.29; N, 14.14%. Found: C, 53.35; H, 4.91; N, 13.76%. Mass analysis: calculated for $C_{22}H_{26}N_5O_3^+BF_4^-$, $C_{22}H_{26}N_5O_3^+$ 408.2030, BF_4^- 87.0035; found, $C_{22}H_{26}N_5O_3^+$ 408.21, BF_4^- 87.01 (Figure S8).

4.2. Thermal Analyses. The phase transition behavior of **1-Bf** was investigated between −30 and 180 °C using a differential scanning calorimeter (Mettler Toledo, DSC-1). Measurements were conducted under a N_2 atmosphere (50 mL min^{-1}) using an aluminum open pan at a scanning rate of ±5.0 °C min^{-1}. The onset temperature of thermal anomaly is defined as the phase transition temperature throughout this work.

Simultaneous powder X-ray diffraction (XRD) and DSC analyses were conducted for the as-prepared **1-Bf** sample using a measurement system comprising an X-ray diffractometer (SmartLab) and differential scanning calorimeter (Rigaku Corporation, Tokyo, Japan). The DSC measurements were taken between 0 and 180 °C at a scanning rate of ±5.0 °C min^{-1} under a N_2 atmosphere (100 mL min^{-1}). The 2θ range for the XRD measurements was set from 5 to 35°, and measurements were taken at 24° min^{-1}, corresponding to a temperature variation of 6.25 °C min^{-1} from the beginning to the end of a single XRD measurement. A monochromatic Cu Kα (λ = 1.541862 Å) radiation was used as the X-ray source.

4.3. Fourier Transform Infrared Spectroscopy (FTIR). FTIR measurements were carried out using an FTIR spectrophotometer (FTS7000e, Agilent). All single-point spectra were recorded at 4 cm^{-1} spectral resolution. Measurements were carried out in the temperature range between 0 and 180 °C at a scanning rate of ±5.0 °C min^{-1} under a N_2 gas flow using a heating/cooling stage (10036L, Japan High Tech Co.). The samples were thinly spared by a sampling knife on a BaF_2 aperture plate.

4.4. Small-Angle X-ray Scattering (SAXS). Small-angle X-ray scattering experiments were performed using beamline BL8S3 at the Aichi Synchrotron Radiation Center, Aichi, Japan. The X-ray wavelength and energy were 0.15 nm and 8.2 keV, respectively, where a camera length of 1170.4 mm was used. An imaging plate (Pilatus 100 k, Dectris, Baden-Daettwil, Switzerland) was used as the detector with an exposure time of 58 s. A scattering vector (q) range of 0.09 to 5.44 nm^{-1} was used, where q is defined as $4\pi\sin\theta/\lambda = 2\pi/d$ (2θ, scattering angle; λ, wavelength; d, diffraction plane distance). The two-dimensional (2D) scattering data were converted to one-dimensional (1D) data based on the q values using the FIT2D software package. A **1-Bf** sample (∼1 mg) was incorporated into a hole (diameter = 3 mm; thickness = 0.6 mm) on the aluminum plate holder. The SAXS measurements were carried out in the temperature range between 0 and 180 °C at a scanning rate of ±5.0 °C min^{-1} under a N_2 atmosphere (50 mL min^{-1}). The 2θ values for SAXS (Figures 2, 4A, and 5A) were converted to those using λ of the Cu Kα radiation.

4.5. Crystallography. To identify the crystal structure of **1-Bf** to serve as references, two sets of single-crystal fragments, an α-Cr (0.07 × 0.04 × 0.03 mm^3) and a β-Cr (0.84 × 0.08 × 0.06 mm^3), were picked up from the product recrystallized in dichloromethane (orange needle-shaped crystals, Sample-I) and in ethanol (yellow crystals, Sample-II), respectively. Similarly, crystal fragments (0.02 × 0.02 × 0.01 mm^3) of Sample-II after DSC analysis and cooled to room temperature (Sample-III) are defined as a cold crystal (cc-Cr).

Single-crystal XRD was conducted by mounting these selected single crystals, namely, the α-Cr, the β-Cr, and the cc-Cr, on the XRD system (Rigaku, XtaLAB Synergy Custom DW system, Tokyo, Japan) equipped with a rotating anode X-ray generator and a hybrid photon counting detector (HyPix-6000). The crystal was held at a constant temperature of −180 °C (93.15 K) during data collection, where ω scans were conducted using Cu Kα radiation. The CrysAlisPro[56] program suite was used for data collection, scaling, multiscan absorption correction, and data reduction. The structure was solved with the ShelXT[57] solution program using dual methods with Olex2[58] as the graphical interface. The model was refined with ShelXL (ver. 2018/3)[59] using the full-matrix least-squares method on $|F|^2$. All non-hydrogen atoms were refined anisotropically, while hydrogen atomic positions were calculated geometrically and refined using the riding hydrogen model.

The Crystallographic Data Centre was used to relate the deposition numbers CCDC-2045382, 2024816, and 2024817 to compounds **1-Bf** (α-Cr), **1-Bf** (β-Cr), and **1-Bf** (cc-Cr). Copies of the data can be obtained free of charge via http://www.ccdc.cam.ac.uk/conts/retrieving.html (or from the Cambridge Crystallographic Data Centre, 12, Union Road, Cambridge, CB21EZ, U.K.; fax: +441223 336033; email: deposit@ccdc.cam.ac.uk).

1-Bf (α-Cr): $C_{22}H_{26}N_5O_3BF_4$, M_w = 495.29, orange needle, monoclinic, space group $P2_1/c$, a = 8.6295(3) Å, b = 18.4095(7) Å, c = 14.6734(6) Å, β = 95.813(4)°, V = 2319.10(15) Å^3, Z = 4, D_{calcd} = 1.419 g cm^{-3}, T = 93.15 K, 12489 reflections collected, 4530 independent (R_{int} = 0.0963), GOF = 1.071, R_1 = 0.0766, wR_2 = 0.2062 for all reflections.

1-Bf (β-Cr): $C_{22}H_{26}N_5O_3BF_4$, M_w = 495.29, yellow block, triclinic, space group P-1, a = 6.2676(3) Å, b = 7.2265(5) Å, c = 25.7041(8) Å, α = 93.703(4)°, β = 91.665(3)°, γ = 94.709(5)°, V = 1157.17(10) Å^3, Z = 2, D_{calcd} = 1.421 g cm^{-3}, T = 93.15 K, 10916 reflections collected, 4491 independent (R_{int} = 0.0437), GOF = 1.050, R_1 = 0.0644, wR_2 = 0.1957 for all reflections.

1-Bf (cc-Cr): $C_{22}H_{26}N_5O_3BF_4$, M_w = 495.29, yellow block, triclinic, space group P-1, a = 6.3153(7) Å, b = 7.2355(11) Å, c = 25.527(3) Å, α = 93.493(12)°, β = 91.539(10)°, γ = 94.822(10)°, V = 1159.6(3) Å^3, Z = 2, D_{calcd} = 1.419 g cm^{-3}, T = 93.15 K, 9357 reflections collected, 2549 independent (R_{int} = 0.1049), GOF = 1.401, R_1 = 0.1414, wR_2 = 0.4499 for all reflections.

4.6. Computational Details. We conducted quantum chemical calculations to elucidate the potential energy landscape of the materials and to analyze the FTIR spectra using the Ganssian09 and Gaussian16 program packages.[60,61] An isolated **1-Bf** molecule optimized under vacuum condition is not a good model of the actual crystal structure because it would not retain its original conformation and the relative

https://doi.org/10.1021/acsomega.1c04866
ACS Omega 2021, 6, 32869−32878

position of the ion pair in the absence of an appropriate packing force. Therefore, for each of α-Cr and β-Cr phases, we employed an 18-molecule cluster model composed of 1 central molecule and 17 peripheral ones. The initial structure was constructed based on the atomic coordinates determined by the single-crystal X-ray analysis, which the structure was refined in the following steps: (1) the geometry of the central molecule was optimized at the HF/6-31G level with the peripheral molecules being fixed, (2) each of the peripheral molecules was replaced with the optimized structure of the central molecule, (3) the central molecule of the thus-obtained structure was optimized with the ONIOM method at the B3LYP/6-311G** and the HF/6-31G levels for the center and the peripheral molecules, respectively, and (4) the processes (2) and (3) were repeated and we confirmed that the difference in total energy was within 2 kJ mol^{-1} per molecule between the first and the final steps of the optimization.[62,63] Thus, we were convinced that we obtained the optimized structures of **1-Bf** in the molecular environment of the given crystal structures, and hence we calculated the normal-mode vibrations to reproduce the IR spectral intensity.

■ ASSOCIATED CONTENT

Supporting Information

The Supporting Information is available free of charge at https://pubs.acs.org/doi/10.1021/acsomega.1c04866.

Crystallographic data of **1-Bf** (α-Cr) (CIF)

Crystallographic data of **1-Bf** (β-Cr) (CIF)

Crystallographic data of **1-Bf** (cc-Cr) (CIF)

Packing structure viewed along the crystallographic *a*-axis and *b*-axis in α-Cr and β-Cr, additional XRD-DSC and DSC charts and numerical summary of thermodynamic quantities, variation in the small angle X-ray scattering (SAXS) of **1-Bf** during the cold crystallization in the second heating process; the ^{1}H NMR and ^{13}C NMR spectra and MALDI-TOF MS spectrum of **1-Bf**, atomic Cartesian coordinates of the L-form molecules in the α-Cr and the SS-form molecules in the β-Cr, whose coordinates were fully optimized using ONIOM with the center and the peripheral molecules at the B3LYP/6-311G** and the HF/6-31G levels, respectively (PDF)

■ AUTHOR INFORMATION

Corresponding Author

Katsunori Iwase − *DENSO CORPORATION, Nisshin, Aichi 470-0111, Japan; Institute of Materials and Systems for Sustainability, Nagoya University, Nagoya, Aichi 464-8601, Japan;* orcid.org/0000-0001-7944-4971; Email: katsunori.iwase.j6h@jp.denso.com

Authors

Katsuma Ishino − *DENSO CORPORATION, Nisshin, Aichi 470-0111, Japan*

Hajime Shingai − *DENSO CORPORATION, Nisshin, Aichi 470-0111, Japan*

Yasuyuki Hikita − *DENSO CORPORATION, Nisshin, Aichi 470-0111, Japan*

Isao Yoshikawa − *Institute of Industrial Science, The University of Tokyo, Tokyo 153-8505, Japan;* orcid.org/0000-0002-9183-7636

Hirohiko Houjou − *Institute of Industrial Science, The University of Tokyo, Tokyo 153-8505, Japan; Environmental Science Center, The University of Tokyo, Tokyo 113-0033, Japan;* orcid.org/0000-0003-3761-9221

Complete contact information is available at: https://pubs.acs.org/10.1021/acsomega.1c04866

Notes

The authors declare no competing financial interest.

■ ACKNOWLEDGMENTS

The authors thank Dr. Yoko Matsuzawa and Dr. Hirokuni Jintoku of the National Institute of Advanced Industrial Science and Technology (AIST) for their valuable opinion regarding the synthesis of ionic liquid crystal materials. We would like to thank Yasuhiro Toyama (DENSO CORP.) for his advice for XRD-DSC analysis. The SAXS experiments were conducted at the BL8S3 of the Aichi Synchrotron Radiation Center, Aichi Science & Technology Foundation, Aichi, Japan (Proposal nos. 202003090 and 202005035). Part of the quantum chemical calculations were carried out using the supercomputer "Flow" at the Information Technology Center, Nagoya University. This research did not receive any specific grant from funding agencies in the public, commercial, or not-for-profit sectors.

■ REFERENCES

(1) Bendova, M.; Canji, M.; Wagner, Z.; Zdolsek, N.; Quirion, F. Phase Transitions in Higher-Melting Ionic Liquids: Thermal Storage Materials or Liquid Crystals? *Chem. Eng. Trans.* **2018**, *69*, 37−42.

(2) Iwase, K.; Nagano, Y.; Yoshikawa, I.; Houjou, H.; Yamamura, Y.; Saito, K. Cold Crystallization in Schiff-Base Nickel(II) Complexes Derived from Three Toluidine Isomers. *J. Phys. Chem. C* **2014**, *118*, 27664−27671.

(3) Turunen, K.; Yazdani, M. R.; Puupponen, S.; Santasalo-Aarnio, A.; Seppälä, A. Cold-crystallizing erythritol-polyelectrolyte: Scaling up reliable long-term heat storage material. *Appl. Energy* **2020**, *266*, 114890−114902.

(4) Yazdani, M. R.; Etula, J.; Zimmerman, J. B.; Seppälä, A. Ionic cross-linked polyvinyl alcohol tunes vitrification and cold-crystallization of sugar alcohol for long-term thermal energy storage. *Green Chem.* **2020**, *22*, 5447−5462.

(5) Tsuji, H.; Bouapao, L. Stereocomplex formation between poly(L-lactic acid) and poly(D-lactic acid) with disproportionately low and high molecular weights from the melt. *Polym. Int.* **2012**, *61*, 442−450.

(6) Shyr, T.-W.; Tung, C.-H.; Cheng, W.-S.; Yang, C.-C. The Crystallization Rate and Morphological Structure of Poly(Ethylene/Trimethylene Terephthlate) Copolyesters under Isothermal Melt-Crystallization and Cold-Crystallization. *J. Polym. Res.* **2013**, *20*, 186.

(7) Henricks, J.; Boyum, M.; Zheng, W. Crystallization Kinetics and Structure Evolution of a Polylactic Acid during Melt and Cold Crystallization. *J. Therm. Anal. Calorim.* **2015**, *120*, 1765−1774.

(8) Endo, T.; Kato, T.; Tozaki, K.; Nishikawa, K. Phase Behaviors of Room Temperature Ionic Liquid Linked with Cation Conformational Changes: 1-Butyl-3-methylimidazolium Hexafluorophosphate. *J. Phys. Chem. B* **2010**, *114*, 407−411.

(9) Efimova, A.; Hubrig, G.; Schmidt, P. Thermal Stability and Crystallization Behavior of Imidazolium Halide Ionic Liquids. *Thermochim. Acta* **2013**, *573*, 162−169.

(10) Kolek, Ł.; Massalska-Arodź, M.; Adrjanowicz, K.; Rozwadowski, T.; Dychtoń, K.; Drajewicz, M.; Kula, P. Molecular Dynamics and Cold Crystallization Process in a Liquid-Crystalline Substance with Para-, Ferro- and Antiferro-Electric Phases as Studied by Dielectric Spectroscopy and Scanning Calorimetry. *J. Mol. Liq.* **2020**, *297*, 111913.

(11) Jasiurkowska-Delaporte, M.; Rozwadowski, T.; Dmochowska, E.; Juszyńska-Gałązka, E.; Kula, P.; Massalska-Arodź, M. Interplay

between Crystallization and Glass Transition in Nematic Liquid Crystal 2,7-Bis(4-pentylphenyl)-9,9-diethyl-9H-fluorene. *J. Phys. Chem. B* **2018**, *122*, 10627−10636.
(12) Rozwadowski, T.; Massalska-Arodź, M.; Kolek, Ł.; Grzybowska, K.; Bąk, A.; Chłędowska, K. Kinetics of Cold Crystallization of 4-Cyano-3-Fluorophenyl 4-Butylbenzoate (4CFPB) Glass Forming Liquid Crystal. I. Nonisothermal Process As Studied by Microscopic, Calorimetric, and Dielectric Methods. *Cryst. Growth Des.* **2015**, *15*, 2891−2900.
(13) Piela, K.; Turowska-Tyrk, I.; Drozd, M.; Szostak, M. M. Polymorphism and Cold Crystallization in Optically Nonlinear N-Benzyl-2-methyl-4-nitroaniline Crystal Studied by X-Ray Diffraction, Calorimetry and Raman Spectroscopy. *J. Mol. Struct.* **2011**, *991*, 42−49.
(14) Sampath, S.; Boopathi, A. A.; Mandal, A. B. "Bottom-up" Self-Assembly and 'Cold Crystallization' of Butterfly Shaped Tetrabenzofluorene Molecules. *Phys. Chem. Chem. Phys.* **2016**, *18*, 21251−21258.
(15) Honda, A.; Takahashi, Y.; Tamaki, Y.; Miyamura, K. Multistep Thermochromism due to Cold Crystallization and Solid−Solid Transition in Alkyl Derivative of Diketo-pyrrolo-pyrrole Pigment. *Chem. Lett.* **2016**, *45*, 211−213.
(16) Kim, S.-J.; Karis, T. E. Glass formation from low molecular weight organic melts. *J. Mater. Res.* **1995**, *10*, 2128−2136.
(17) Kimijima, A.; Honda, A.; Nomoto, K.; Miyamura, K. Cold crystallization in the mixed system of adenine and thymine dodecyl derivatives. *CrystEngComm* **2019**, *21*, 3142−3145.
(18) Iwase, K.; Yoshikawa, I.; Houjou, H.; Yamamura, Y.; Saito, K. Structural Isomerization and Cold Crystallization of Bis[1-(2-propyl)iminomethylnaphthalen-2-olato]nickel(II) by Thermal Analysis, X-ray Diffraction, and FT-IR. *Bull. Chem. Soc. Jpn.* **2015**, *88*, 989−995.
(19) Iwase, K.; Toyama, Y.; Yoshikawa, I.; Yamamura, Y.; Saito; Houjou, H. Insight into Structural Demand for Cold Crystallization of a Small Molecule. A Case Study for Schiff Base Compounds that Exhibit Prototropic Tautomerization. *Bull. Chem. Soc. Jpn.* **2018**, *91*, 669−677.
(20) Arai, N.; Sorai, M.; Seki, S. Calorimetric and Magnetic Studies of Crystalline and Glassy Bis[N-(3-methoxysalicylidene)-isopropylamine]nickel(II). *Bull. Chem. Soc. Jpn.* **1972**, *45*, 2398−2406.
(21) Wang, Q.; Takeuchi, A.; Yamamura, Y.; Saito, K.; Mori, W.; Sorai, M. Thermodynamic Relationship Between Structural Isomers of the Thermochromic Compound Bis(N-isopropyl-5,6-benzosalicylideneiminato)nickel(II). *J. Phys. Chem. B* **2008**, *112*, 11039−11048.
(22) Rezvani, Z.; Abbasi, A. R.; Nejati, K.; Seyedahmadian, M. Syntheses, characterization and glass-forming properties of new bis[5-((4-ndodecyloxyphenyl)azo)-N-(4-nalkoxyphenyl)-salicylaldiminato]-nickel (II) complex homologues. *Polyhedron* **2005**, *24*, 1461−1470.
(23) Shirota, Y. Organic materials for electronic and optoelectronic devices. *J. Mater. Chem.* **2000**, *10*, 1−25.
(24) Das, S. P.; Ganguly, R.; Li, Y.; Soo, H. S. Nucleophilic Reactivity and Electrocatalytic Reduction of Halogenated Organic Compounds by Nickel o-Phenylenedioxamidate Complexes. *Dalton Trans.* **2016**, *45*, 13556−13564.
(25) Achira, H.; Yoshikawa, I.; Houjou, H. Supercooling and Cold Crystallization of Ni-salphen Complexes by Hybridization with Bis(Ni-salphen) Containing a Semiflexible Linker. *Chem. Lett.* **2016**, *45*, 1415−1417.
(26) Honda, A.; Yoshida, T.; Shioda, A.; Nomoto, K.; Miyamura, K. Cold Crystallization of Chiral Schiff-Base Nickel(II) Complex Having Alkyl Chains and a Characteristic Methyl Group. *Bull. Chem. Soc. Jpn.* **2019**, *92*, 1853−1858.
(27) Kato, T.; Uchida, J.; Ichikawa, T.; Sakamoto, T. Functional Liquid Crystals towards The Next Generation of Materials. *Angew. Chem., Int. Ed.* **2018**, *57*, 4355−4371.
(28) Dai, J.; Majhi, D.; Kharkov, B. B.; Dvinskikh, S. V. NMR Spectroscopic Study of Orientational Order in Imidazolium-Based Ionic Liquid Crystals. *Crystals* 2019, *9*, 495.
(29) Saielli, G. The effect of hydration on the stability of ionic liquid crystals: MD simulations of $[C_{14}C_1im]Cl$ and $[C_{14}C_1im]Cl{\cdot}H_2O$. *Phys. Chem. Chem. Phys.* **2021**, 24386.
(30) Kolmangadi, M. A.; Yildirim, A.; Sentker, K.; Butschies, M.; Bühlmeyer, A.; Huber, P.; Laschat, S.; Schönhals, A. Molecular dynamics and electrical conductivity of Guanidinium based ionic liquid crystals: Influence of cation headgroup configuration. *J. Mol. Liq.* **2021**, *330*, 115666.
(31) Saielli, G. Special Issue Editorial: Ionic Liquid Crystals. *Crystals* **2019**, *9*, 274.
(32) Salikolimi, K.; Sudhakar, A. A.; Ishida, Y. Functional ionic liquid crystals. *Langmuir* **2020**, *36*, 11702−11731.
(33) Goossens, K.; Lava, K.; Bielawski, C. W.; Binnemans, K. Ionic Liquid Crystals: Versatile Materials. *Chem. Rev.* **2016**, *116*, 4643−4807.
(34) Stappert, K.; Muthmann, J.; Spielberg, E. T.; Mudring, A.-V. Azobenzene-Based Organic Salts with Ionic Liquid and Liquid Crystalline Properties. *Cryst. Growth Des.* **2015**, *15*, 4701−4712.
(35) Vraneš, M.; Papović, S.; Rackov, S.; Alenezi, K.; Gadžurić, S.; Tot, A.; Pilić, B. Thermophysical and electrochemical properties of 1−alkyl−3−(3−butenyl) imidazolium bromide ionic liquids. *J. Chem. Thermodyn.* **2019**, *139*, 1−11.
(36) Abe, H. Phase variety in ionic liquids: Hydrogen bonding and molecular conformations. *J. Mol. Liq.* **2021**, *332*, 115189−115227.
(37) Zhang, Q.; Jiao, L.; Shan, C.; Hou, P.; Chen, B.; Xu, X.; Niu, L. Synthesis and characterisation of novel imidazolium-based ionic liquid crystals with a p-nitroazobenzene moiety. *Liq. Cryst.* **2008**, *35*, 765−772.
(38) Singh, S. K.; Savoy, A. W. Ionic Liquids Synthesis and Applications: An Overview. *J. Mol. Liq.* **2020**, *297*, 112038.
(39) Keaveney, S. T.; Haines, R. S.; Harper, J. B. Ionic liquid solvents: the importance of microscopic interactions in predicting organic reaction outcomes. *Pure Appl. Chem.* **2017**, *89*, 745−757.
(40) Guglielmero, L.; Mezzetta, A.; Pomelli, C. S.; Chiappe, C.; Guazzelli, L. Evaluation of the effect of the dicationic ionic liquid structure on the cycloaddition of CO_2 to epoxides. *J. CO Util.* **2019**, *34*, 437−445.
(41) Claus, J.; Sommer, F. O.; Kragl, U. Ionic liquids in biotechnology and beyond. *Solid State Ionics* **2018**, *314*, 119−128.
(42) Martins, V. L.; Torresi, R. M. Ionic liquids in electrochemical energy storage. *Curr. Opin. Electrochem.* **2018**, *9*, 26−32.
(43) Trujillo-Rodríguez, M. J.; Nan, H.; Varona, M.; Emaus, M. N.; Souza, I. D.; Anderson, J. L. Advances of Ionic Liquids in Analytical Chemistry. *Anal. Chem.* **2019**, *91*, 505−531.
(44) Welton, T. Ionic liquid: a brief history. *Biophys. Rev.* **2018**, *10*, 691−706.
(45) New Energy and Industrial Technology Development Organization (NEDO., Japan), https://www.nedo.go.jp/news/press/AA5_101074.html (accessed December 26, 2020).
(46) Sakka, S.; Makenzie, J. D. Relation between Apparent Glass Transition Temperature and Liquidus Temperature for Inorganic Glasses. *J. Non-Cryst. Solids* **1971**, *6*, 145−162.
(47) Sakka, S. Oxynitride Glasses. *Annu. Rev. Mater. Sci.* **1986**, *16*, 29−46.
(48) Alba, C.; Fan, J.; Angell, C. A. Thermodynamic aspects of the glass transition phenomenon. II. Molecular liquids with variable interactions. *J. Chem. Phys.* **1999**, *110*, 5262−5272.
(49) MacRae, C. F.; Sovago, I.; Cottrell, S. J.; Galek, P. T. A.; McCabe, P.; Pidcock, E.; Platings, M.; Shields, G. P.; Stevens, J. S.; Towler, M.; Wood, P. A. Mercury 4.0: From Visualization to Analysis, Design and Prediction. *J. Appl. Crystallogr.* **2020**, *53*, 226−235.
(50) Turnbull, D. Formation of Crystal Nuclei in Liquid Metals. *J. Appl. Phys.* **1950**, *21*, 1022−1028.
(51) Boistelle, R.; Astier, J. P. Crystallization mechanisms in solution. *J. Cryst. Growth* **1988**, *90*, 14−30.
(52) Deb, D.; Bhattacharya, S. Influence of ionic-liquid-tethered Al_2O_3 nanoparticle on the nonisothermal cold crystallization in ionic -liquid-based nanofluids. *J. Phys. Chem. C* **2017**, *121*, 6962−6976.

https://doi.org/10.1021/acsomega.1c04866
ACS Omega 2021, 6, 32869−32878

(53) Vyazovkin, S. *Physical Processes. Isoconversional Kinetics of Thermally Stimulated Processes*. Springer International Publishing:-Cham, 2015; 63−161, DOI: 10.1007/978-3-319-14175-6_3.
(54) Roth, C.; Chatzipapadopoulos, S.; Kerle, D.; Friedriszik, F.; Lutgens, M.; Lochbrunner, S.; Kuhn, O.; Ludwig, R. Hydrogen Bonding in Ionic Liquids Probed by Linear and Nonlinear Vibrational Spectroscopy. *New J. Phys.* **2012**, *14*, 105026−105041.
(55) Köddermann, T.; Wertz, C.; Heintz, A.; Ludwig, R. Ion-Pair Formation in the Ionic Liquid 1-Ethyl-3-Methylimidazolium Bis-(Triflyl)Imide as a Function of Temperature and Concentration. *ChemPhysChem* **2006**, *7*, 1944−1949.
(56) Rigaku Oxford Diffraction. *CrysAlisPro Software System* (ver. 1.171.41.76a); 171.39; Rigaku Oxford Diffraction: Oxford, UK, 2017.
(57) Sheldrick, G. Crystal structure refinement with SHELXL. *Acta Crystallogr., Sect. C: Struct. Chem.* **2015**, *71*, 3−8.
(58) Dolomanov, O. V.; Bourhis, L. J.; Gildea, R. J.; Howard, J. A. K.; Puschmann, H. OLEX2: a complete structure solution, refinement and analysis program. *J. Appl. Crystallogr.* **2009**, *42*, 339−341.
(59) Sheldrick, G. M. *Acta Crystallogr., Sect. A: Found. Adv.* **2015**, *71*, 3−8.
(60) Frisch, M. J.; Trucks, G. W.; Schlegel, H. B.; Scuseria, G. E.; Robb, M. A.; Cheeseman, J. R.; Scalmani, G.; Barone, V.; Mennucci, B.; Petersson, G. A.; Nakatsuji, H.; Caricato, M.; Li, X.; Hratchian, H. P.; Izmaylov, A. F.; Bloino, J.; Zheng, G.; Sonnenberg, J. L.; Hada, M.; Ehara, M.; Toyota, K.; Fukuda, R.; Hasegawa, J.; Ishida, M.; Nakajima, T.; Honda, Y.; Kitao, O.; Nakai, H.; Vreven, T.; Montgomery, J. A., Jr.; Peralta, J. E.; Ogliaro, F.; Bearpark, M.; Heyd, J. J.; Brothers, E.; Kudin, K. N.; Staroverov, V. N.; Kobayashi, R.; Normand, J.; Raghavachari, K.; Rendell, A.; Burant, J. C.; Iyengar, S. S.; Tomasi, J.; Cossi, M.; Rega, N.; Millam, N. J.; Klene, M.; Knox, J. E.; Cross, J. B.; Bakken, V.; Adamo, C.; Jaramillo, J.; Gomperts, R.; Stratmann, R. E.; Yazyev, O.; Austin, A. J.; Cammi, R.; Pomelli, C.; Ochterski, J. W.; Martin, R. L.; Morokuma, K.; Zakrzewski, V. G.; Voth, G. A.; Salvador, P.; Dannenberg, J. J.; Dapprich, S.; Daniels, A. D.; Farkas, Ö.; Foresman, J. B.; Ortiz, J. V.; Cioslowski, J.; Fox, D. J. *Gaussian 09*, Revision D.01, Gaussian, Inc., Wallingford CT, 2013.
(61) Frisch, M. J.; Trucks, G. W.; Schlegel, H. B.; Scuseria, G. E.; Robb, M. A.; Cheeseman, J. R.; Scalmani, G.; Barone, V.; Petersson, G. A.; Nakatsuji, H.; Li, X.; Caricato, M.; Marenich, A. V.; Bloino, J.; Janesko, B. G.; Gomperts, R.; Mennucci, B.; Hratchian, H. P.; Ortiz, J. V.; Izmaylov, A. F.; Sonnenberg, J. L.; Williams-Young, D.; Ding, F.; Lipparini, F.; Egidi, F.; Goings, J.; Peng, B.; Petrone, A.; Henderson, T.; Ranasinghe, D.; Zakrzewski, V. G.; Gao, J.; Rega, N.; Zheng, G.; Liang, W.; Hada, M.; Ehara, M.; Toyota, K.; Fukuda, R.; Hasegawa, J.; Ishida, M.; Nakajima, T.; Honda, Y.; Kitao, O.; Nakai, H.; Vreven, T.; Throssell, K.; Montgomery, J. A., Jr.; Peralta, J. E.; Ogliaro, F.; Bearpark, M. J.; Heyd, J. J.; Brothers, E. N.; Kudin, K. N.; Staroverov, V. N.; Keith, T. A.; Kobayashi, R.; Normand, J.; Raghavachari, K.; Rendell, A. P.; Burant, J. C.; Iyengar, S. S.; Tomasi, J.; Cossi, M.; Millam, J. M.; Klene, M.; Adamo, C.; Cammi, R.; Ochterski, J. W.; Martin, R. L.; Morokuma, K.; Farkas, O.; Foresman, J. B.; Fox, D. J. *Gaussian 16*, Revision C.01, Gaussian, Inc., Wallingford CT, 2019.
(62) Dapprich, S.; Komáromi, I.; Byun, S.; Morokuma, K.; Frisch, M. J. A new ONIOM implementation in Gaussian 98. Part I. the calculations of energies, gradients, vibrational frequencies, and electric field deviratives. *J. Mol. Struct.: THEOCHEM* **1999**, *461*, 1−21.
(63) Svensson, M.; Humbel, S.; Froese, R. D. J.; Matsubara, J.; Siber, S.; Morokuma, K. ONIOM: a multilayered integrated MO + MM method for geometry optimizations and single point energy predictions. a test for Diels−Alder reactions and $Pt(P(t\text{-}Bu)_3)_2$ + H_2 oxidative addition. *J. Phys. Chem.* **1996**, *100*, 19357−19363.

https://doi.org/10.1021/acsomega.1c04866
ACS Omega 2021, 6, 32869−32878